Check for updates

Cu/Au-doped nanopolymers with multiple catalytic activities for NIR II laser-promoted nanocatalytic tumor therapy†

Xixi Wu,[a] Xiang Feng,[a] Peng Yu,[c] Jing Zhang[d] and Rui Liu [ID] *[b]

Breast cancer remains a significant global health concern owing to the limitations of conventional therapies, such as side effects, drug resistance, and high costs. Nanocatalytic therapy has emerged as a promising alternative due to its tumor specificity, spatiotemporal controllability, and noninvasiveness. However, its effectiveness is limited by endogenous antioxidants like glutathione (GSH) and the low catalytic activity of nanocatalysts. Herein, an Cu/Au-doped polypyrrole nanocatalyst, Cu-AuPP, with multiple catalytic activities is developed by sequentially polymerizing pyrrole monomers using $CuCl_2$ and $HAuCl_4$, followed by PEGylation. The obtained Cu-AuPP catalyzes the production of hydroxyl radicals ($\cdot$OH) and facilitates the oxidation of GSH to GSSG *via* redox reactions mediated by multivalent Cu ions, leading to oxidative damage, mitochondrial dysfunction, and tumor cell apoptosis. Upon 1064 nm laser irradiation, these catalytic activities were enhanced by elevated temperature and electron–hole separation mediated by Au nanoclusters, resulting in more intense oxidative damage to tumor cells. Collectively, the developed Cu-AuPP nanocatalytic medicine capable of simultaneously catalyzing GSH depletion and $\cdot$OH production *via* several improved catalytic mechanisms, has significant promise for the treatment of malignant tumors.

1. Introduction

Breast cancer remains a major health challenge for women globally, characterized by high mortality rates.[1] Conventional therapies, including surgery, radiotherapy, chemotherapy, and immunotherapy, often yield suboptimal outcomes due to issues such as invasiveness, advanced side effects, drug resistance, and high costs.[2–4] Recent advancements have highlighted nanocatalytic therapy as a promising alternative owing to its tumor specificity, spatiotemporal controllability, and noninvasive features.[5–7] By harnessing the unique tumor microenvironment and metabolic differences between tumor cells and normal cells, nanocatalysts demonstrate specific catalytic activity to generate reactive oxygen species (ROS) within tumor cells, consequently diminishing interference to normal physiological processes and minimizing toxicity to healthy tissues,

[a]Department of Radiation Oncology, The People's Hospital of Guangxi Zhuang Autonomous Region, Nanning 530000, China
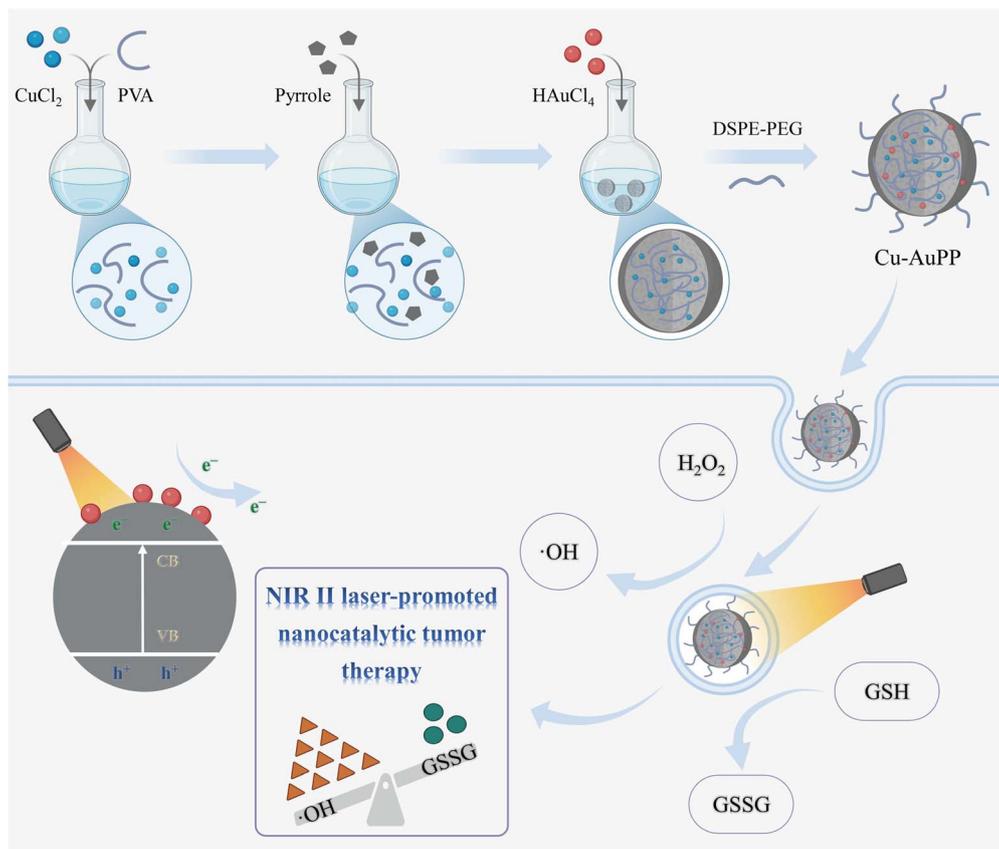
[b]Department of Joint Surgery and Sports Medicine, The People's Hospital of Guangxi Zhuang Autonomous Region, Nanning 530000, China. E-mail: lr1021231810@163. com

[c]Department of Endocrinology and Metabolism, The Second Affiliated Hospital, Jiangxi Medical College, Nanchang University, Nanchang, Jiangxi, 330006, China

[d]Department of Anesthesiology, The Second Affiliated Hospital, Jiangxi Medical College, Nanchang University, Nanchang, Jiangxi Province, 330006, China

† Electronic supplementary information (ESI) available. See DOI: https://doi.org/10.1039/d4ra08591d

a major drawback of traditional chemical drugs.[8,9] For instance, Fe-based nanocatalysts utilize excess hydrogen peroxide (H_2O_2) in tumor cells as a substrate to catalyze the production of hydroxyl radicals ($\cdot$OH), which selectively eradicate tumor cells in a process known as Fenton catalytic therapy.[10–12] Despite its potential for tumor suppression, nanocatalytic therapy often necessitates high dosages to counteract limited catalytic activity and endogenous antioxidants in tumors, such as glutathione (GSH), thereby raising the risk of toxicity.[13–15] As a result, improving the effectiveness of nanocatalytic therapy is a critical concern for ensuring safety and efficacy.

To date, various strategies have been developed and implemented to improve nanocatalytic therapeutics. Studies have demonstrated that Cu-based nanocatalysts have superior catalytic activity with less dependency on harsh conditions in comparison to Fe-based nanocatalysts.[16–18] Incorporating noble metals as electron acceptors at interfaces or blocks to promote ROS generation by increasing electron–hole separation is also an effective strategy to improve catalytic activity.[19–21] Among these, gold (Au) with excellent electrical conductivity has received great interest.[22,23] Furthermore, numerous studies have showed that a controlled increase in local temperature is contributed to catalytic processes.[24,25] The merging of laser and photothermal agents permits spatiotemporal selectivity and accelerates catalytic rate, a strategy that has been applied in oncology.[26] Due to the practical challenges related to the restricted tissue penetration of ultraviolet and near-infrared (NIR) lasers, NIR II laser-

Scheme 1 Schematic illustration of the fabrication of Cu-AuPP and its multiple catalytic mechanism for NIR II laser-enhanced nanocatalytic tumor therapy.

responsive compounds have more potential for clinical therapeutic applications.[27,28] Additionally, intratumoral GSH levels increase spontaneously in response to ROS generation, alleviating oxidative stress damage in tumor cells.[29] Conversely, artificially manipulating GSH levels in tumors may alleviate the constraints on oxidative stress damage and boost nanocatalytic therapy. Therefore, modulating antioxidant levels in tumors while augmenting the catalytic activity of nanocatalysts is a potent approach to enhance nanocatalytic therapy.

Polypyrrole (PPy) is a widely studied heterocyclic conjugated conductive polymer made by electrochemical or oxidant-initiated polymerization of pyrrole monomers or their derivatives.[30] PPy demonstrates advantageous properties such as biocompatibility, stability, electrical conductivity, and strong optical absorption coupled with high photothermal conversion efficiency.[31–33] In our prior investigation, tetrachloroauric acid (HAuCl$_4$) was utilized as an oxidant to synthesis Au-doped PPy (AuP), which exhibited significant optical absorption and photothermal effects in the NIR I and II regions.[34] However, the catalytic activity of AuP remains unknown, despite the common use of Au monomers as electron acceptors in catalytic fields. Recent research has focused on improving the physicochemical properties and physiological activities of PPy by optimizing the oxidant and stabilizer components, while introducing novel therapeutic functions.[35,36] For instance, multivalent Cu-doped

PPy has been successfully synthesized using copper chloride (CuCl$_2$) as an oxidant, effectively inducing oxidative stress in tumor tissues and activating immune responses.[37]

Inspired by these findings, we developed here a technique to initiate the polymerization of pyrrole monomers using HAuCl$_4$ and CuCl$_2$ in a sequential manner (Scheme 1). This process involved the partial reduction of HAuCl$_4$ and CuCl$_2$ to form Au nanoclusters and Cu$^+$ ions, which were subsequently incorporated into PPy nanostructures. The resulting composite was further modified by DSPE-PEG to produce Cu-AuPP, wherein DSPE-PEG modification improved its physiological stability. Compared to the previously reported PEGylated AuP (AuPP), Cu-AuPP not only improved photothermal conversion efficiency but also exhibited a range of catalytic activities, including GSH consumption and ROS generation. Upon reaching the tumor site, Cu$^+$/Cu^{2+} ions embedded inside the nanostructures catalyzed the conversion of GSH and H$_2$O$_2$ into oxidized glutathione (GSSG) and ·OH, respectively, which process was further accelerated by the photothermal effect induced by the NIR II laser. Simultaneously, Au nanoclusters functioned as electron acceptors to augment catalytic activities during irradiation, leading to increased ·OH production and more intense oxidative damage to tumor cells. Collectively, this engineered Cu-AuPP showed significant promise for advancing tumor nanocatalytic therapy.

2. Experimental section

2.1. Materials and chemicals

Polyvinyl alcohol (PVA), pyrrole, copper chloride (CuCl$_2$), and glutathione (GSH) were purchased from Aladdin. Tetrachloroauric acid trihydrate (HAuCl$_4 \cdot$3H$_2$O), methylene blue (MB), 5,5-dimethyl-1-pyrroline oxide (DMPO), and 5,5′-dithiobis (2-nitrobenzoic acid) (DTNB) were sourced from Sigma-Aldrich. 1,2-Distearoyl-*sn-glycero*-3-phosphoethanolamine-*N* [amino-(polyethylene glycol) 2000] (DSPE-PEG, molecular weight: 2000) was supplied by Xi'an Ruixi Biotech Biochemistry Technology Co., Ltd. 2′,7′-Dichlorofluorescin diacetateb (DCFH-DA), calcein-AM, propidium iodide (PI), and JC-1 probes were obtained from Beyotime Biotechnology. ThiolTracker™ Violet was bought from ThermoFisher Scientific. Dulbecco's modified eagle's medium (DMEM), phosphate buffer (PBS), fetal bovine serum, and trypsin–EDTA were obtained from Gibco-BRL.

2.2. Synthesis of Cu-AuP

50 mg of PVA were dissolved in 10 mL of deionized (Di) water inside a 100 mL round-bottom flask and stirred for 1 h at 90 °C. The solution was then allowed to cool naturally to room temperature, after which 75 mg mL^{-1} CuCl$_2$ (10 mL) was slowly added and stirred for 0.5 h. Following that, 200 μL of pyrrole monomer was added to the mixture and stirred for 12 h. Then, 5 mM HAuCl$_4 \cdot$3H$_2$O solution (5 mL) was added dropwise and stirred continuously for 1 h. The precipitate was collected by centrifuging the resultant mixture for 20 min at 20 000 rpm, and it was then rinsed three times with Di water.

2.3. Synthesis of Cu-AuPP

In an ice bath sonication environment, 10 mg of Cu-AuP was dissolved in 10 mL of Di water. Subsequently, 50 mg of DSPE-PEG was added, followed by mixing and sonication for 0.5 h. After stirring for 24 h, the product was centrifuged and rinsed with Di water to purify Cu-AuPP.

2.4. Characterization

Transmission electron microscopy (TEM, JEM-2100UHR, Japan) was used to investigate the nanocatalyst morphology. The chemical components and crystal structures were examined using X-ray photoelectron spectroscopy (XPS, ESCALAB 250Xi, Japan), X-ray diffraction (XRD, Bruker D8, Germany), and a Fourier transform infrared spectrometer (FTIR, Nexus 470, USA). Thermal images and temperature changes were recorded using a thermal imaging camera (FlukeTi100, USA). The optical absorption was investigated using a UV-vis-NIR spectrometer (Infinite M200 Pro, Switzerland). Dynamic light scattering (DLS, NanoBrook 173Plus, USA) was used to measure dynamic particle size and zeta potential.

2.5. Photothermal conversion performance

The temperature variations of Cu-AuPP was recorded over time using an infrared camera to evaluate its photothermal conversion efficiency. Cu-AuPP solutions at various concentrations (0, 6.25, 12.5, 25, and 50 μg mL^{-1}) were subjected to a 1064 nm laser at various power densities (0.5, 1.0, 1.5, and 2.0 W cm^{-2}) for 5 min, with pure water serving as a control. Photothermal stability was assessed by exposing Cu-AuPP (25 μg mL^{-1}) to a 1064 nm laser (1.0 W cm^{-2}) for five cycles of alternating 6 min of irradiation and 6 min of rest. Furthermore, the photothermal conversion efficiency was examined by exposing Cu-AuPP (25 μg mL^{-1}) to a 1064 nm laser (1.0 W cm^{-2}) for 15 min, and then cooling it for another 15 min.

2.6. *In vitro* GSH depletion and ·OH generation

A DTNB probe and UV-vis-NIR spectroscopy were used to examine the GSH depletion of Cu-AuPP. Briefly, either AuPP or Cu-AuPP (25 μg mL^{-1}) was added to a GSH solution (1 mM) and incubated at 37 °C. After 20 min of incubation, a 1064 nm laser (1.0 W cm^{-2}) was administered for 5 minutes to the groups that needed irradiation. The mixtures were extracted and mixed with DTNB (10 mg mL^{-1}) after 60 min of co-incubation. UV-vis-NIR spectroscopy was then used to quantify the absorbance of the resultant suspensions.

The ·OH generation of Cu-AuPP was analyzed utilizing a MB probe and UV-vis-NIR spectroscopy. Briefly, either AuPP or Cu-AuPP (25 μg mL^{-1}) was added to the mixed solutions of 7 μg mL^{-1} of MB and 5 mM of H$_2$O$_2$. The groups that needed laser treatment were exposed to 1064 nm laser irradiation (1.0 W cm^{-2}) for 5 min after co-incubation for 0, 15, 30, 45, and 60 min. Using a UV-vis-NIR spectrometer, the absorbance of those mixtures was detected every 15 min. To further determine ·OH generation, Cu-AuPP was mixed with H$_2$O$_2$ (5 mM) and DMPO probe, either with or without 1064 nm laser irradiation. Electron spin resonance was then used to capture the ·OH signal.

2.7. Intracellular GSH depletion and ·OH generation

ThiolTracker™ Violet and DCFH-DA probes were employed to detect variations in GSH and ·OH levels in mouse breast cancer cells (4T1 cells). Mouse breast cancer cells (4T1 cells) were purchased from the American Type Culture Collection (ATCC). Briefly, 4T1 cells (2×10^5 cells per dish) were seeded in confocal dishes and incubated overnight. The cells were treated with pure DMEM, AuPP, or Cu-AuPP after PBS washing. The cells in the laser-treated group were subjected to a 1064 nm laser at 1.0 W cm^{-2} for 5 min. After 12 h of incubation, the medium was replaced with DMEM containing either ThiolTracker™ Violet (20 μM) or DCFH-DA (10 μM), and incubated for 30 min. Subsequently, the cells were rinsed with PBS, fixed with 4% paraformaldehyde, stained with DAPI, and imaged using a confocal laser scanning microscope (CLSM, FV3000, Japan).

2.8. Cellular uptake

4T1 cells (2×10^5 cells per dish) were seeded in confocal dishes and incubated overnight at 37 °C. The cells were treated with Cy5-labeled Cu-AuPP (Cy5: 5 μg mL^{-1}) diluted in DMEM after PBS washing. Following incubation periods of 1, 3, and 6 h, the old medium was removed, the samples were rinsed with PBS, and then imaged using CLSM.

2.9. Cell cytotoxicity

The cytotoxicity of Cu-AuPP on 4T1 cells was assessed using the conventional cell counting kit-8 (CCK-8) test. Briefly, 4T1 cells were seeded at a density of 5×10^3 cells per well onto 96-well plates, and then incubated overnight. Fresh DMEM with various concentrations of Cu-AuPP (0, 7.5, 15, 30, and 60 µg mL^{-1}) was added to replace the old medium. After 12 h of co-incubation, the cells in the groups needing laser treatment were subjected to a 1064 nm laser (1.0 W cm^{-2}, 5 min), followed by an additional 12 h of incubation. Finally, the cell viability was determined with the CCK-8 procedure.

The NIR II laser-promoted therapeutic effects of Cu-AuPP were investigated in 4T1 cells using calcein-AM/PI staining. 4T1 cells were seeded in 24-well plates and incubated overnight. Fresh DMEM, with or without Cu-AuPP (30 µg mL^{-1}), was added to replace the old medium and incubated for 24 h. The cells in the laser-treated groups underwent 1064 nm laser irradiation (1.0 W cm^{-2}, 5 min). Subsequently, each well was filled with calcein-AM and PI, and the mixture was incubated for 20 min. Following PBS washing, a fluorescence microscope was used to observe the cells.

2.10. Mitochondrial membrane potential

Mitochondrial membrane potential assay was performed using the JC-1 probe. 4T1 cells were seeded in confocal dishes at a density of 2×10^5 cells per dish and incubated overnight. The cells were then exposed to either pure DMEM or Cu-AuPP (30 µg mL^{-1}) for 12 h. The cells in the laser-treated groups underwent 1064 nm laser irradiation (1.0 W cm^{-2}, 5 min). Images were obtained using CLSM after the cells were stained with JC-1 dye for 15 min.

2.11. Statistical analysis

All statistical analyses were performed using GraphPad Prism software. The results of statistical analysis were presented as mean ± SD. Statistical significance was calculated by one-way ANOVA analysis. The statistical significance was defined as $*p < 0.05$; $**p < 0.01$; $***p < 0.001$.

3. Results and discussion

3.1. Synthesis and characterization

In the manufacture of Cu-AuP, CuCl$_2$ was employed as the primary oxidant to initiate the oxidative polymerization of pyrrole monomer, with PVA acting as a stabilizer. Subsequently, HAuCl$_4$ was introduced as a secondary oxidant to accelerate polymerization while reducing to Au nanoclusters. Fig. 1a and c illustrated the spherical morphology of the synthesized Cu-AuP nanoparticles, which possessed a hydrodynamic diameter of approximately 125.6 nm, as shown by TEM images and DLS measurements. Following PEGylated modification, the spherical morphology of Cu-AuPP remained consistent, but its hydrodynamic diameter and zeta potential changed to approximately 169.9 nm and −5.26 mV, respectively, as indicated by the DLS data (Fig. 1b and d). The hydrodynamic diameters of Cu-AuPP in DMEM medium at different pH levels remained constant within 48 h, indicating the good stability of Cu-AuPP (Fig. S1†). The crystal structure of Cu-AuP was analyzed using XRD spectroscopy, which displayed the characteristic diffraction peaks of cubic Au (JCPDS no. 04-0784), confirming the successful reduction of HAuCl$_4$ to Au nanoclusters (Fig. 1e). Additionally, a broad diffraction peak in the range of 24° to 35° was observed, corresponding to the
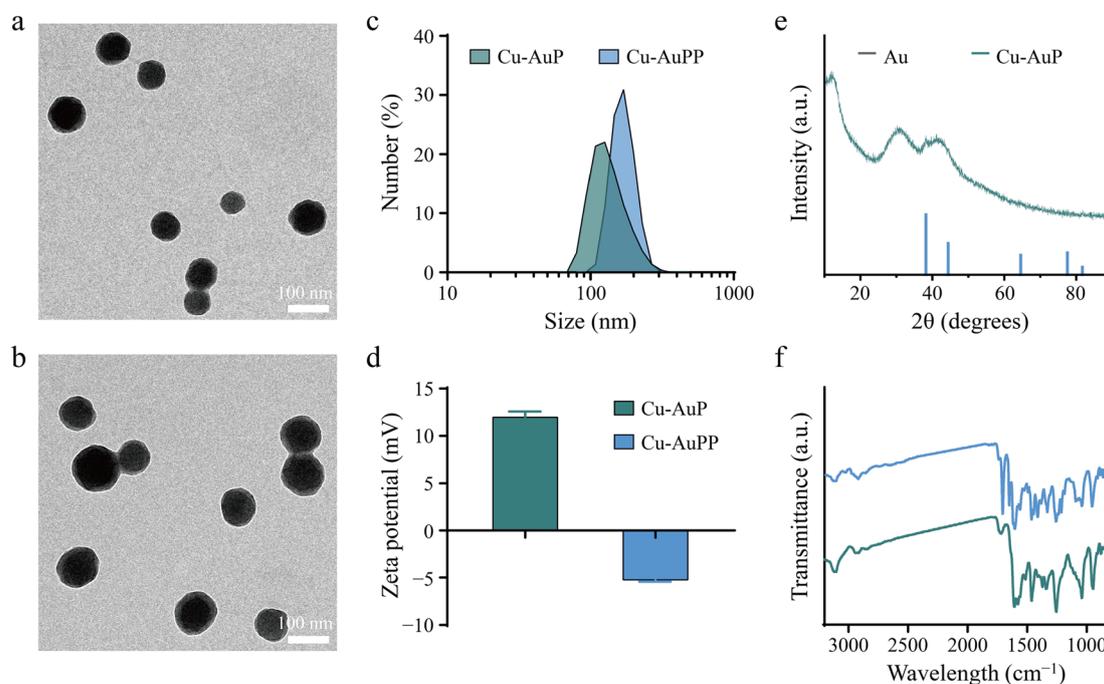

Fig. 1 TEM images of (a) Cu–AuP and (b) Cu–AuPP. (c) Size distribution and (d) zeta potential of Cu–AuP and Cu–AuPP. (e) XRD spectra of Cu–AuP. (f) FTIR spectra of Cu–AuP and Cu–AuPP.
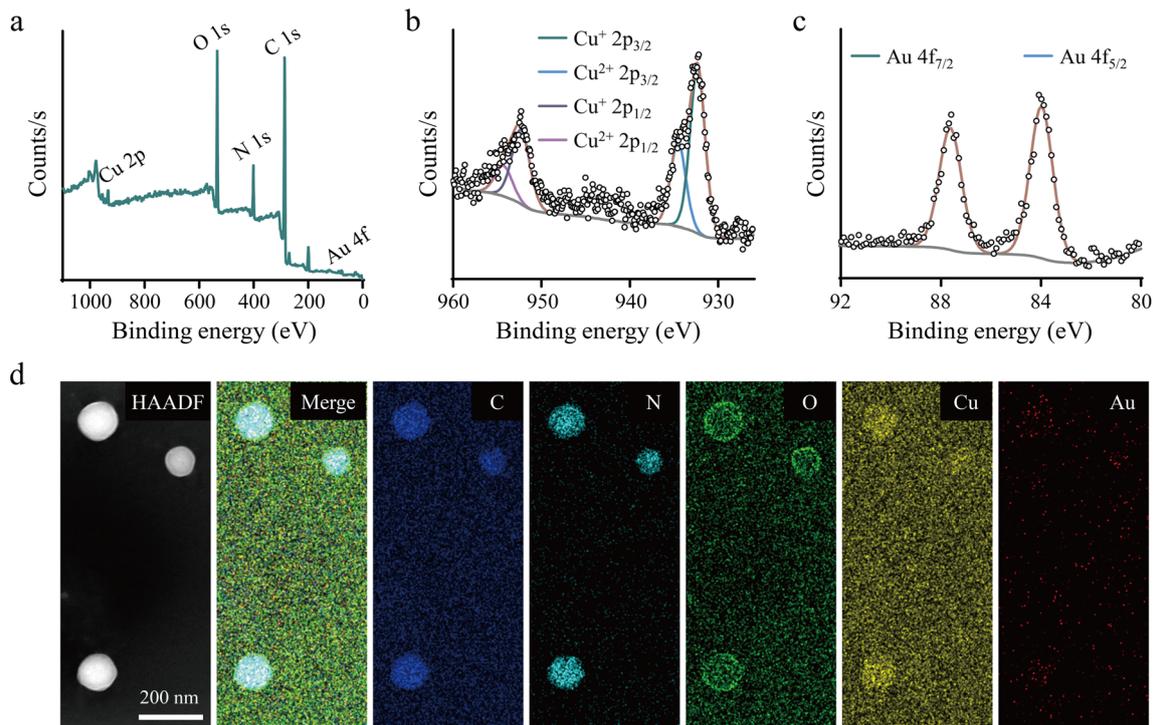
Fig. 2 (a) The full XPS spectra of Cu-AuP. The corresponding high-resolution XPS spectra of (b) Cu 2p and (c) Au 4f. (d) High-resolution TEM images and corresponding elemental mapping images of Cu-AuP.

intermolecular stacking structures characteristic of amorphous PPy. In the FTIR spectra, distinct peaks at 1257, 1462, and 1609 cm^{-1} were detected in both Cu-AuP and Cu-AuPP, corresponding to C–H, C–N, and C≡N stretching vibrations typical of PPy frameworks, indicating the presence of PPy structures (Fig. 1f).
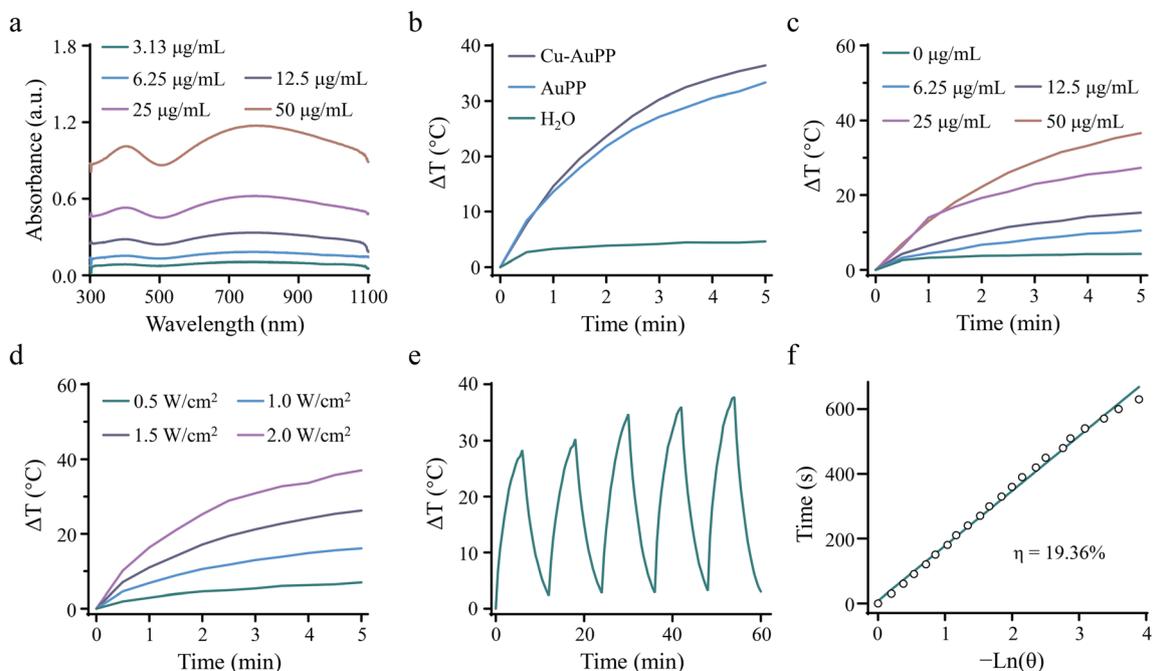

Fig. 3 (a) UV-vis-NIR absorbance spectra of different concentrations of Cu-AuPP. (b) Temperature rise curve of H$_2$O, AuPP, and Cu-AuPP under 1064 nm laser irradiation (1.0 W cm^{-2}). (c) Temperature rise curve of different concentrations of Cu-AuPP under 1064 nm laser irradiation (1.0 W cm^{-2}). (d) Temperature rise curve of Cu-AuPP at different laser power densities (0.5, 1.0, 1.5, and 2.0 W cm^{-2}). (e) Heating curves of the Cu-AuPP dispersion in DI water for five laser ON/OFF cycles (1064 nm, 1.0 W cm^{-2}). (f) The linear relationship between time and −ln θ from the cooling period.

Next, XPS detection was conducted to analyze the chemical constitution of Cu-AuPP. The elements C, N, O, Au, and Cu were identified in Cu-AuP, verifying the effective co-doping of Au nanoclusters and Cu ions (Fig. 2a). High-resolution XPS spectra was used to further investigate the chemical states of these elements. Both monovalent and divalent Cu states were identifiable in the Cu 2p XPS spectra, with peaks at 932.3 eV and 934.5 eV attributed to Cu^+ $2p_{3/2}$ and Cu^{2+} $2p_{3/2}$, respectively, and peaks at 952.3 and 954.3 eV belonging to Cu^+ $2p_{1/2}$ and Cu^{2+} $2p_{1/2}$, respectively (Fig. 2b). The Cu^+ to Cu^{2+} ratio in Cu-AuP was calculated as 2.98 : 1. The formation of Au nanoclusters was confirmed by the characteristic peaks at 83.9 eV and 87.6 eV corresponding to Au $4f_{7/2}$ and Au $4f_{5/2}$, respectively, in the high-resolution Au 4f spectra (Fig. 2c). Furthermore, the high-resolution C 1s spectra had four peaks at 284.0, 284.8, 286.3, and 287.8 eV, which corresponded to Cα, Cβ, C=N/C–N$^+$, and C=O in the PPy structure, respectively. Similarly, pyrrolic N, C–N$^+$, and C=N$^+$ in PPy were identified as three peaks at 399.6, 401.2, and 402.8 eV in the high-resolution N 1s spectra (Fig. S2†). These findings confirmed the presence of the PPy nanostructure in Cu-AuP, with Cu ions predominantly existing in monovalent and divalent states, and Au forming nanoclusters. High-resolution TEM and elemental mapping images further revealed the homogeneous and overlapping distribution of C, N, O, Au, and Cu elements in Cu-AuP (Fig. 2d).

3.2. Optical absorption and photothermal property of Cu-AuPP

The broad absorption of Cu-AuPP in the NIR I and II regions was validated by recording its UV-vis-NIR spectra at various concentrations (Fig. 3a). The absorbance at 1064 nm displayed a linear increase with concentration, indicating the efficient optical energy harvesting capability of Cu-AuPP nanocatalysts from 1064 nm laser irradiation (Fig. S3†). A thermal camera was then employed to monitor the temperature rise (ΔT) of AuPP and Cu-AuPP solutions under 1064 nm laser irradiation. Following 5 min of laser irradiation at 1.0 W cm^{-2}, the ΔT for AuPP and Cu-AuPP solutions were 33.32 and 36.40 °C, respectively, whereas the ΔT for H$_2$O, serving as a control, was negligible (Fig. 3b and S4a†). Moreover, the photothermal curves of Cu-AuPP exhibited a pattern depending on both concentration and power density (Fig. 3c and d). For instance, the ΔT of Cu-AuPP solution at concentrations of 25 and 50 μg mL^{-1} rose to 27.26 and 36.59 °C, respectively, after 5 min of irradiation (1.0 W cm^{-2}). The photostability of Cu-AuPP was then evaluated by a repetitive laser activation and deactivation protocol. As

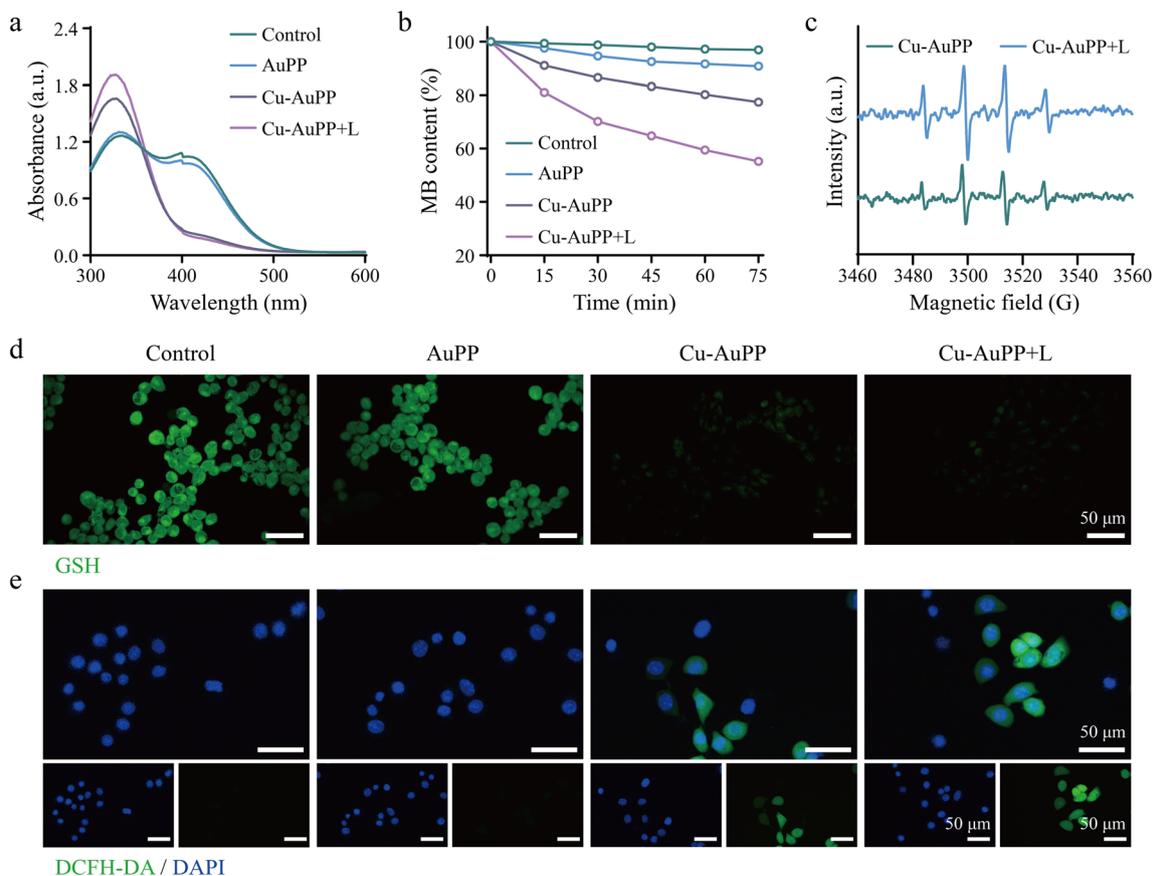Fig. 4 (a) The GSH degradation caused by different samples. (b) The MB degradation in different sample solutions containing H$_2$O$_2$ (5 mM), with or without 1064 nm laser irradiation. (c) ESR spectra of ·OH radicals trapped by DMPO in different sample solutions, with or without 1064 nm laser irradiation. CLSM images of intracellular (d) GSH depletion and (e) ·OH generation in 4T1 cells treated with AuPP, Cu-AuPP, or Cu-AuPP + L.

shown in Fig. 3e, the temperature profile of Cu-AuPP under irradiation remained stable over five consecutive on/off cycles, demonstrating good photothermal stability of Cu-AuPP. The photothermal conversion efficiency (η) of Cu-AuPP under 1064 nm laser irradiation was calculated to be 19.36%, comparable to that of previously reported conjugated polymer (20.2%)[38] and PPy-based hydrogel (20.3%)[39] (Fig. 3f and S4b†). Together, these findings well confirmed the prominent photothermal conversion property of Cu-AuPP.

3.3. Multiple catalytic activities of Cu-AuPP

To demonstrate the multiple catalytic activities of Cu-AuPP, DTNB probe was initially utilized as a GSH indicator to assess residual GSH levels by detecting the formation of yellow 5-mercapto-2-nitrobenzoic acid (TNB), which exhibited a characteristic absorption peak at 412 nm. In comparison to AuPP, Cu-AuPP showed significantly greater GSH depletion during an identical 1 h incubation, as evidenced by the lower absorbance intensity of TNB at 412 nm (Fig. 4a). This catalytic capability was

ascribed to the redox reaction between Cu^{2+} active sites and GSH. More importantly, laser irradiation further amplified this catalytic activity, likely owing to the facilitation of redox processes driven by electron migration mediated by Au nanoclusters (Fig. S5†). After that, the Fenton catalytic activity of Cu-AuPP, with and without 1064 nm laser irradiation, was investigated using MB as an indicator. Fig. 4b illustrated a gradual reduction in MB levels in the Cu-AuPP group, indicating the generation of ·OH through a Cu^{+}-driven Fenton catalytic reaction. Laser-induced photoelectron generation and migration further boosted ·OH generation in the Cu-AuPP + L group. Moreover, electron spin resonance (ESR) approach was used to track the generation of ·OH by employing DMPO as a spin-trapping agent. As shown in Fig. 4c, the characteristic signal of the ·OH/DMPO adduct was identified as a quadruple signal with a relative intensity of 1 : 2 : 2 : 1, in the ESR spectrum, confirming laser-enhanced ·OH production via Cu-AuPP-mediated catalytic reactions.

Encouraged by the superior catalytic activity of Cu-AuPP in a simulated tumor microenvironment, we then assessed its
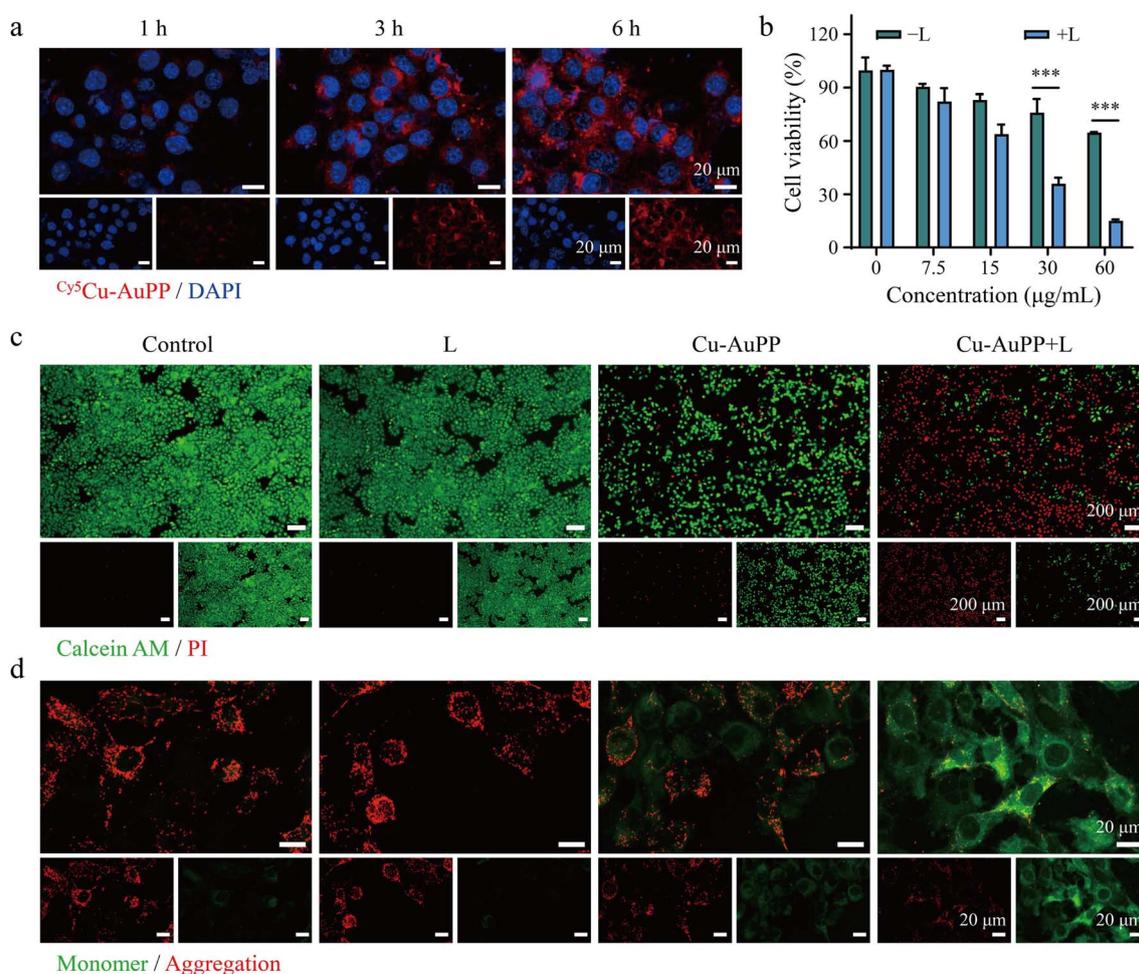

Fig. 5 (a) CLSM images of 4T1 cells after incubation with Cy5Cu-AuPP for different periods. (b) Relative cell viability of 4T1 cells after treatment with different concentrations of Cu-AuPP, with or without 1064 nm laser irradiation. (c) Calcein-AM and PI staining to identify live/dead cells (green: live, red: dead) after different treatments. (d) CLSM images of mitochondrial membrane potential in 4T1 cells after different treatments. Statistical significance was calculated by one-way ANOVA analysis. *$P < 0.05$, **$P < 0.01$, ***$P < 0.001$.

catalytic properties on mouse breast cancer 4T1 cells using ThiolTracker™ Violet and DCFH-DA fluorescence probes. As displayed in Fig. 4d, untreated 4T1 cells exhibited strong green fluorescence, indicating high GSH levels within tumor cells. After incubation with Cu-AuPP for 12 h, 4T1 cells demonstrated decreased fluorescence, whereas the AuPP group showed comparable fluorescent intensity to that of the control group. Importantly, the green fluorescence was further diminished in the Cu-AuPP + L group, which demonstrated the enhanced GSH depletion *via* hyperthermia-accelerated Cu^{2+}-mediated redox reactions. Subsequently, the ·OH generation in 4T1 cells was determined using DCFH-DA probe, which emits green fluorescence upon oxidation by ·OH. As shown in Fig. 4e, negligible green fluorescence was found in both the control and AuPP groups, whereas the Cu-AuPP group showed increased green fluorescence attributable to Cu^+/Cu^{2+}-mediated multiple catalytic processes. Significantly, the cells treated with Cu-AuPP + L exhibited the greatest ·OH fluorescence signal, which was attributed to increased catalytic activity induced by hyperthermia.

3.4. Cellular uptake and antitumor effect

The intracellular distribution of Cy5-labeled Cu-AuPP (^{Cy5}Cu-AuPP) was examined using CLSM. A steady rise in red fluorescence over time indicated a time-dependent cellular uptake of ^{Cy5}Cu-AuPP, as displayed in Fig. 5a. Subsequently, the therapeutic effects of Cu-AuPP under 1064 nm laser irradiation were evaluated *via* standard CCK-8, live/dead cell staining, and JC-1 staining assays. Following a 24 h incubation of Cu-AuPP with 4T1 cells, cell survival decreased in a concentration-dependent manner, highlighting the multiple catalytic activities of Cu-AuPP within tumor cells (Fig. 5b). Upon exposure to the 1064 nm laser, the CCK-8 assay demonstrated a notable reduction in 4T1 cell viability. Specifically, the cell survival decreased to 35.97% and 14.99% at concentrations of 30 and 60 μg mL^{-1}, respectively, which was attributed to the NIR II laser-accelerated catalytic activity of Cu-AuPP. Additionally, fluorescence imaging of live/dead cells further confirmed the excellent antitumor efficacy mediated by Cu-AuPP and amplified by 1064 nm laser irradiation (Fig. 5c). Compared to the control, laser-only, and Cu-AuPP-only groups, the Cu-AuPP + L-treated cells showed a significant decrease in live cells (green fluorescence) and an increase in dead cells (red fluorescence) following 5 minutes of laser exposure. The JC-1 indicator, which displayed red aggregates when the mitochondrial membrane potential was normal and green when depolarized, was next used to assess probable mitochondrial malfunction after various treatments. Consistent with the live/dead staining results, the green/red fluorescence intensity ratio was elevated in the Cu-AuPP group, and further augmented after laser irradiation, indicating severe mitochondrial dysfunction due to oxidative damage (Fig. 5d).

4. Conclusions

In summary, we have developed an Cu-AuPP nanocatalyst with multiple catalytic activities for NIR II laser-enhanced nanocatalytic tumor therapy. In comparison with our previously reported AuPP, Cu-AuPP resulting from the sequential polymerization of pyrrole monomers using $HAuCl_4$ and $CuCl_2$ exhibited a range of catalytic activities, including the generation of ·OH from excessive H_2O_2 and the conversion of GSH to GSSG within tumor cells. These activities were primarily ascribed to the doped multivalent Cu ions. More importantly, NIR II laser irradiation enhanced these catalytic activities, presumably due to the promotion of redox processes driven by elevated temperature and electron migration. Collectively, these catalytic reactions induced oxidative stress and damage in tumor cells, as evidenced by live/dead cell staining and mitochondrial membrane potential assays. The Cu-AuPP produced in this study offers a promising alternative for nanocatalysts by enhancing catalytic activity and depleting GSH, thus advancing the development of nanocatalytic nanomedicines for tumor therapy.

Data availability

All relevant data are within the manuscript and its additional files.

Author contributions

R. L. conceptualized and designed the research; X. W., X. F., and P. Y. performed the experiments and analyzed the data. J. Z. contributed to some cellular experiments. X. W. and R. L. wrote the manuscript. All authors contributed to the discussion of the results and implications, and revising of the manuscript at all stages. All authors have given approval to the final version of the manuscript.

Conflicts of interest

There are no conflicts to declare.

Acknowledgements

References

1 N. Harbeck, F. Penault-Llorca, J. Cortes, M. Gnant, N. Houssami, P. Poortmans, K. Ruddy, J. Tsang and F. Cardoso, *Nat. Rev. Dis. Primers*, 2019, **5**, 66.
2 S. K. Yeo and J. L. Guan, *Trends Cancer*, 2017, **3**, 753–760.
3 M. R. Lloyd, K. Jhaveri, K. Kalinsky, A. Bardia and S. A. Wander, *Nat. Rev. Clin. Oncol.*, 2024, **21**, 743–761.

4 W. Zeng, H. Zhang, Y. Deng, A. Jiang, X. Bao, M. Guo, Z. Li, M. Wu, X. Ji, X. Zeng and L. Mei, *Chem. Eng. J.*, 2020, **389**, 124494.

5 W. Zeng, H. Zhang, X. Yuan, T. Chen, Z. Pei and X. Ji, *Adv. Drug Delivery Rev.*, 2022, **184**, 114241.

6 W. Feng, X. Han, R. Wang, X. Gao, P. Hu, W. Yue, Y. Chen and J. Shi, *Adv. Mater.*, 2019, **31**, 1805919.

7 B. Yang, Y. Chen and J. Shi, *Adv. Mater.*, 2019, **31**, 1901778.

8 Y. Kang, Z. Mao, Y. Wang, C. Pan, M. Ou, H. Zhang, W. Zeng and X. Ji, *Nat. Commun.*, 2022, **13**, 2425.

9 Y. Nie, W. Zhang, W. Xiao, W. Zeng, T. Chen, W. Huang, X. Wu, Y. Kang, J. Dong, W. Luo and X. Ji, *Biomaterials*, 2022, **289**, 121791.

10 Z. Tang, Y. Liu, M. He and W. Bu, *Angew. Chem., Int. Ed.*, 2019, **58**, 946–956.

11 M. Huo, L. Wang, Y. Wang, Y. Chen and J. Shi, *ACS Nano*, 2019, **13**, 2643–2653.

12 Y. Wang, D. Wang, Y. Zhang, H. Xu, L. Shen, J. Cheng, X. Xu, H. Tan, X. Chen and J. Li, *Bioact. Mater.*, 2023, **22**, 239–253.

13 Z. Jie, B. Xiong and J. Shi, *Adv. Sci.*, 2024, **11**, 2402801.

14 Y. Li, W. Fan, X. Gu, S. Liu, T. He, S. Gou, W. Meng, M. Li, X. Liu, Y. Ren, C. Qi and K. Cai, *Adv. Funct. Mater.*, 2024, **34**, 2313540.

15 Y. He, X. Liu, L. Xing, X. Wan, X. Chang and H. Jiang, *Biomaterials*, 2020, **241**, 119911.

16 C. Huang, J. Tang, Y. Liu, T. Chen, J. Qi, S. Sun, H. Hao, W. Zeng, J. Zhao and M. Wu, *Acta Biomater.*, 2023, **167**, 463–472.

17 W. Li, Y. Xiao, N. Zhu, Z. Chen, Z. Jiang, B. Li, G. Yu, Z. Guo, M. Liang and W. Guo, *Nano Today*, 2024, **56**, 102223.

18 L. Fu, Y. Wan, C. Qi, J. He, C. Li, C. Yang, H. Xu, J. Lin and P. Huang, *Adv. Mater.*, 2021, **33**, 2006892.

19 X. Meng, H. Fan, L. Chen, J. He, C. Hong, J. Xie, Y. Hou, K. Wang, X. Gao, L. Gao, X. Yan and K. Fan, *Nat. Commun.*, 2024, **15**, 1626.

20 Y. Xu, M. Fan, W. Yang, Y. Xiao, L. Zeng, X. Wu, Q. Xu, C. Su and Q. He, *Adv. Mater.*, 2021, **33**, 2101455.

21 X. Wu, Y. Li, M. Wen, Y. Xie, K. Zeng, Y. Liu, W. Chen and Y. Zhao, *Chem. Soc. Rev.*, 2024, **53**, 2643–2692.

22 T. Chen, W. Zeng, C. Tie, M. Yu, H. Hao, Y. Deng, Q. Li, H. Zheng, M. Wu and L. Mei, *Bioact. Mater.*, 2022, **10**, 515–525.

23 L. Cai, J. Du, F. Han, T. Shi, H. Zhang, Y. Lu, S. Long, W. Sun, J. Fan and X. Peng, *ACS Nano*, 2023, **17**, 7901–7910.

24 J. Hao, K. Ge, G. Chen, B. Dai and Y. Li, *Chem. Soc. Rev.*, 2023, **52**, 7707–7736.

25 J. Lou-Franco, B. Das, C. Elliott and C. Cao, *Nano-Micro Lett.*, 2021, **13**, 10.

26 Y. Yao, W. Zeng, H. Ping, X. Zeng and M. Lin, *View*, 2021, **2**, 20200042.

27 H. Zhang, W. Zeng, C. Pan, L. Feng, M. Ou, X. Zeng, X. Liang, M. Wu, X. Ji and L. Mei, *Adv. Funct. Mater.*, 2019, **29**, 1903791.

28 C. Li, G. Chen, Y. Zhang, F. Wu and Q. Wang, *J. Am. Chem. Soc.*, 2020, **142**, 14789–14804.

29 Y. Xiong, C. Xiao, Z. Li and X. Yang, *Chem. Soc. Rev.*, 2021, **50**, 6013–6041.

30 L. Hao, C. Dong, L. Zhang, K. Zhu and D. Yu, *Polymers*, 2022, **14**, 5139.

31 W. Zeng, X. Wu, T. Chen, S. Sun, Z. Shi, J. Liu, X. Ji, X. Zeng, J. Guan, L. Mei and M. Wu, *Adv. Funct. Mater.*, 2021, **31**, 2008362.

32 Y. Liu, Y. Yi, S. Sun, T. Wang, J. Tang, Z. Peng, W. Huang, W. Zeng and M. Wu, *Small*, 2024, **20**, 2309206.

33 L. Wang, G. Liu, Y. Hu, S. Gou, T. He, Q. Feng and K. Cai, *Nanoscale*, 2022, **14**, 3097–3111.

34 X. Wu, H. Liang, C. Li, D. Zhou and R. Liu, *RSC Adv.*, 2023, **13**, 29061–29069.

35 H. Li, Y. Li, L. Su, K. Zheng, Y. Zhang, J. Li, F. Lv, M. Huang, T. Chen, H. Zhang, Z. Shi, D. Zhu, X. Dong, W. Zeng and L. Mei, *Adv. Sci.*, 2024, **11**, 2308250.

36 Y. Wang, W. Zeng, H. Liang, X. Wu, H. Li, T. Chen, M. Yang, X. Wang, W. Li, F. Zhang, Q. Li, F. Ye, J. Guan and L. Mei, *ACS Appl. Mater. Interfaces*, 2022, **14**, 50557–50568.

37 W. Zeng, M. Yu, T. Chen, Y. Liu, Y. Yi, C. Huang, J. Tang, H. Li, M. Ou, T. Wang, M. Wu and L. Mei, *Adv. Sci.*, 2022, **9**, 2201703.

38 G. Zhang, Y. Dai, D. Wang, Y. Liu, H. Lu, L. Qiu and K. Cho, *Dyes Pigm.*, 2017, **147**, 175–182.

39 S. Geng, H. Zhao, G. Zhan, Y. Zhao and X. Yang, *ACS Appl. Mater. Interfaces*, 2020, **12**, 7995–8005.